*aerospace*

MDPI

*Article*

# Anti-Icing System Performance Prediction Using POD and PSO-BP Neural Networks

**Handong Mao [1], Xiaodan Lin [1,*], Zhimao Li [1], Xiaobin Shen [2] and Wenzhao Zhao [2]**

[1] Environmental Control and Oxygen System Department, COMAC Shanghai Aircraft Design and Research Institute, Shanghai 201210, China; maohandong@comac.cc (H.M.); lizhimao@comac.cc (Z.L.)
[2] Laboratory of Fundamental Science on Ergonomics and Environmental Control, School of Aeronautic Science and Engineering, Beihang University, Beijing 100191, China; shenxiaobin@buaa.edu.cn (X.S.); zhaowenzhao@buaa.edu.cn (W.Z.)
* Correspondence: linxiaodan@comac.cc; Tel.: +86-132-5080-8073

**Abstract:** The anti-icing system is important for ice protection and flight safety. Rapid prediction of the anti-icing system's performance is critical to reducing the design time and increasing efficiency. The paper proposes a method to quickly predict the anti-icing performance of the hot air anti-icing system. The method is based on Proper Orthogonal Decomposition (POD) and Back Propagation (BP) neural networks improved with the Particle Swarm Optimization (PSO) algorithm to construct the PSO-BP neural network. POD is utilized for data compression and feature extraction for the skin temperature and runback water obtained by numerical calculation. A lower-dimensional approximation is derived from the projection subspace, which consists of a set of basis modes. The PSO-BP neural network establishes the mapping relationship between the flight condition parameters (including flight height, atmospheric temperature, flight speed, median volume diameter, and liquid water content) and the characteristic coefficients. The results show that the average absolute errors of prediction with the PSO-BP neural network model on skin temperature and runback water thickness are 3.87 K and 0.93 μm, respectively. The method can provide an effective tool for iteratively optimizing hot air anti-icing system design.

**Keywords:** anti-icing system; BP neural network; PSO optimization algorithm; POD; skin temperature; runback water



**Citation:** Mao, H.; Lin, X.; Li, Z.; Shen, X.; Zhao, W. Anti-Icing System Performance Prediction Using POD and PSO-BP Neural Networks. *Aerospace* **2024**, *11*, 430. https://doi.org/10.3390/aerospace11060430

Academic Editor: Konstantinos Kontis

Received: 12 March 2024
Revised: 22 May 2024
Accepted: 23 May 2024
Published: 26 May 2024



## 1. Introduction

Aircraft icing occurs when supercooled droplets that may be present in clouds at air temperatures below freezing are caught on the windward surfaces of components during flight, such as the wings and engine inlet. Ice accumulation has great damage to the aerodynamic characteristics of aircraft, resulting in reduced lift by 30% and increased drag by 40% [1–3], and even causing flight accidents [4]. Therefore, anti-icing systems or de-icing systems are essential for protecting aircraft from ice accumulation for a safe flight. The hot air anti-icing system is widely used in the aircraft industry [5,6], where hot bleed airflow induced by the engine is discharged from the holes of the piccolo tube installed at the wing leading edge to heat the skin surface. However, it will result in increasing engine fuel consumption, reducing engine thrust, and wasting large amounts of energy. It is necessary to carry out iterative optimization of the hot air anti-icing system design to enhance the design efficiency and minimize energy consumption.

Advanced numerical simulation of thermal anti-icing systems has been highly anticipated as a supplementary design and certification tool, in addition to anti-icing experiments and flight tests [7–9]. Modeling and numerical simulation for hot air anti-icing system design is a complex problem involving multiphase flow, conjugate heat, and mass transfer with phase change [10]. The calculation of the flow field and temperature field with high accuracy requires a significant amount of computational time, which increases as the grid

number increases. Aircraft icing conditions vary vastly for anti-icing system design. The factors mentioned above result in a significant increase in computing time for anti-icing system performance. Therefore, it is essential to establish an effective method to obtain skin temperature and the runback water distribution of other icing conditions from the existing computational or experimental data quickly.

Recently, artificial neural networks (ANNs) have greatly advanced research in extracting data features with strong adaptivity, learning ability, and fault tolerance [11]. It can accurately approximate the complex nonlinear function mapping relationships between data and learn the essential characteristics of data from a limited sample set. ANN has been widely used in air temperature prediction as part of weather prediction [12,13], sea surface temperature prediction [14–16], and water temperature prediction [17]. Meanwhile, the prediction of asphalt pavement water film thickness with ANN [18] and the thickness of liquid films on corrugated plate walls with the back propagation (BP) neural network [19] also demonstrate the power of neural networks. As to aircraft wing anti-icing and de-icing applications, ANN have been widely used for fast prediction of ice shape [20–23], in-flight parameters for icing detection [24–26], aircraft icing severity [27], icing probability [28], skin temperature [29], and runback water flow [30]. Ogretim E. [20] proposed a method of ice shape fast prediction using a neural network with icing conditions as input and ice shape parameters as output. The experimental data on ice accretion in the NACA 0012 wing model were used as the training sample sets for the neural network. Chang et al. [21] presented a new technique that combines wavelet packet transform (WPT) and ANN to predict ice accretion on the surface of an airfoil. Results showed an advantage of WPT in performing the analysis of ice accretion information, and the prediction accuracy was improved as well. Strijhak et al. [23] discussed the procedure and method for the ice accretion prediction for different airfoils using ANNs, which were based on the results of the numerical experiments and performed well. Yiqun Dong [24] applied a deep neural network to identify and characterize aircraft icing for in-flight parameter detection. In [27], the authors introduced a purely data-driven approach to finding the complex pattern between different flight conditions and aircraft icing severity prediction using machine learning based on the Extreme Gradient Boosting (XGBoost) algorithm. Abdelghany et al. [29] presented a novel approach based on machine learning (ML) and the Internet of Things (IoT) to predict the thermal performance characteristics of a partial span wing anti-icing system constructed using the NACA 23014 airfoil section. A high-precision computation of skin temperature and runback water thickness relies on a large grid number. Therefore, using anti-icing performance datasets with higher dimensionality as the training samples of the neural network will result in significantly increased computing time.

Proper Orthogonal Decomposition (POD) is a powerful method for order reduction and data compression. It offers an efficient way to capture the dominant features of a system with multiple degrees of freedom and represent the desired precision using a relevant set of modes, thereby reducing the order of the system [31,32]. Skin temperature, runback water thickness, and other anti-icing performance parameters can be decomposed into the basis modes that express data characteristics with POD. Then, the linear fitting coefficients needed to reconstruct the anti-icing performance are obtained using the basis modes [30]. As a result, the high-dimensional datasets with anti-icing performance can be downgraded to low-dimensional samples of fitting coefficients, leading to a significant reduction in computing time and data storage space. Habashi et al. [33] established a fast prediction model of aircraft 3D icing ice shape based on POD, and the results showed that the POD method can improve prediction accuracy by 600~800 times. SungKi Jung et al. [34] used POD for dimensionality reduction and integrated it with a neural network to accurately predict the collection efficiency and ice accretion shapes on an airfoil.

In this paper, a fast prediction model for the performance of a hot air anti-icing system based on POD and PSO-BP neural networks that combine BP neural networks with Particle Swarm Optimization (PSO) is proposed. The anti-icing performance, including skin temperature and runback water thickness, is obtained through numerical simulation

using FENSAP-ICE as the original datasets. The high-dimensional icing performance data are then order-reduced by POD to attain the basis modes and characteristic coefficients. Finally, the PSO-BP neural network is used to establish the mapping relationship between the flight condition parameters, including flight height, atmospheric temperature, flight speed, median volume diameter (MVD), and liquid water content (LWC), and the characteristic coefficient above, which realizes a fast prediction of the hot air anti-icing system performance under various flight icing conditions.

## 2. Methodology

### *2.1. Proper Orthogonal Decomposition*

The Proper Orthogonal Decomposition method allows a series of basis modes to be obtained based on the observed complex physical field. For a sample of the target information field $\boldsymbol{U} = \left\{\boldsymbol{U}^1, \ldots, \boldsymbol{U}^i, \ldots, \boldsymbol{U}^M\right\}$, $\boldsymbol{U}^i$ represents a set of data for the information field. The sample $\boldsymbol{U}$ is a snapshot matrix of order $N \times M$, where $N$ represents the dimension of the data sample $\boldsymbol{U}^i$, i.e., the number of the grid nodes in Computational Fluid Dynamics (CFD). The essence of the POD algorithm is to find a set of optimal orthogonal basis $\boldsymbol{\psi}$ such that the information field of a sample can be represented by its linear representation as follows [32]:

$$\boldsymbol{U}^i = \sum_{j=1}^{M} \alpha_j^i \cdot \boldsymbol{\psi}^j, \tag{1}$$

where $\alpha_j^i$ is the orthogonal basis coefficient, and $\boldsymbol{\psi}^j$ is the orthogonal basis. All $\boldsymbol{\psi}^j$ form an optimal orthogonal basis matrix, and the optimal orthogonal basis satisfies that the average value of the projections of all samples on the optimal basis is maximized. Since the optimal orthogonal basis matrix $\boldsymbol{\psi}$ is of the same order as the sample matrix $\boldsymbol{U}$, it can be expressed as follows:

$$\boldsymbol{\psi} = \boldsymbol{U} \cdot \boldsymbol{V}, \tag{2}$$

where the matrix $\boldsymbol{V}$ is the matrix consisting of the eigenvectors of the matrix $\boldsymbol{C}$, and it satisfies the following:

$$\boldsymbol{C} \cdot \boldsymbol{V} = \boldsymbol{\Lambda} \cdot \boldsymbol{V}. \tag{3}$$

$\boldsymbol{\Lambda}$ is the eigenvalue of the matrix $\boldsymbol{C}$ that can be computed from the sample matrix as follows:

$$\boldsymbol{C}_{ij} = \frac{1}{M} \sum_{k=1}^{N} \boldsymbol{U}_k^i \boldsymbol{U}_k^j. \tag{4}$$

Then the sample matrix can be expressed as a linear superposition of the basis modes. The eigenvalue reflects the proportion of energy in the corresponding basis mode in the sample [31]. Sorting the eigenvectors of matrix $\boldsymbol{C}$ in descending order of the corresponding eigenvalues, the energy of the flow field in the direction of the $j$th optimal orthogonal basis as a proportion of the total energy is as follows:

$$E_n / E_{total} = \sum_{j=1}^{n} \lambda_j / \sum_{j=1}^{N} \lambda_j, \tag{5}$$

where $\lambda_j$ stands for the corresponding eigenvalue of the $j$th basis mode. It can realize the sample dimensionality reduction by ignoring some basis modes with smaller energy and selecting the reserved basis modes according to the energy proportion.

### *2.2. PSO-BP Neural Network*

#### 2.2.1. BP Neural Network

The BP neural network is a multilayer forward neural network trained with the error backpropagation algorithm [35], which consists of an input layer, hidden layers, and an output layer connected sequentially. A typical BP neural network is shown in Figure 1. $x_1$,

$x_2, \ldots, x_m$ are the inputs of the neural network; $v_{hi}$ denotes the connection weight between the input layer and the hidden layer; $a_1, a_2, \ldots, a_g, \ldots, a_q$ are the inputs of the neurons in the hidden layer; $b_1, b_2, \ldots, b_g, \ldots, b_q$ are the outputs of the neurons in the hidden layer; $w_{kh}$ is the connection weight between the hidden layer and the output layer; $\beta_1, \ldots, \beta_n$ are the inputs of the neurons in the output layer; and $y_1, \ldots, y_n$ are the outputs of the neural network.

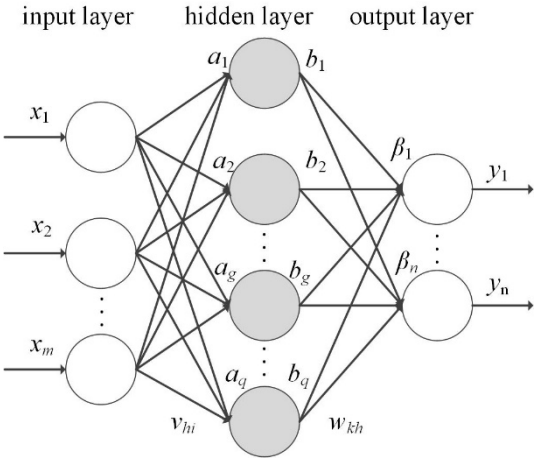


**Figure 1.** Typical BP neural network structure.

The training process of a BP neural network includes forward propagation of the work signal and back propagation of errors. The main steps are described as follows:

Step 1: Initially, the connection weights and thresholds of the BP neural network are randomly initialized in the range (0, 1).

Step 2: Input the training datasets $\boldsymbol{X}$ and compute the input $a_h$ and the output $b_h$ of each neuron in the hidden layer, as well as the input $\beta_k$ and output $y_k$ of each neuron in the output layer.

$$\begin{aligned} a_h &= \sum_{i=1}^{m} v_{hi} x_i \\ b_h &= f(a_h - \gamma_h), \quad h = 1, 2, \ldots, g, \ldots, q \end{aligned} \tag{6}$$

$$\begin{aligned} \beta_k &= \sum_{h=1}^{q} w_{kh} b_h \\ y_k &= f(\beta_k - \theta_k), \quad k = 1, 2, \ldots, n \end{aligned} \tag{7}$$

where $\gamma_h$ is the threshold of the $h$th neuron in the hidden layer; $q$ represents the number of neurons in the hidden layer; $\theta_k$ is the threshold of the $k$th neuron in the output layer; $n$ stands for the number of neurons in the output layer; and $f$ is the activation function.

Step 3: Calculate the mean square error $e$ of a neural network. If the mean square error $e$ is less than or equal to the target computational accuracy of the neural network $\varepsilon$, the neural network training will be completed; conversely, training needs to continue.

$$e = \frac{1}{n} \sum_{k=1}^{n} (y_k - \hat{y}_k)^2 \tag{8}$$

Step 4: The error signal is back propagated. The connection weights and thresholds of the output layer are adjusted according to the output error signal $e$.

$$\frac{\partial e}{\partial w_{kh}} = \frac{\partial e}{\partial y_k} \frac{\partial y_k}{\partial \beta_k} \frac{\partial \beta_k}{\partial w_{kh}} = y_k(1 - y_k)(\hat{y}_k - y_k) b_h \tag{9}$$

$$\frac{\partial e}{\partial \delta_k} = \frac{\partial e}{\partial y_k} \frac{\partial y_k}{\partial \delta_k} = -y_k(1 - y_k)(\hat{y}_k - y_k) \tag{10}$$

$$w_{kh} = w_{kh} + \Delta w_{kh} = w_{kh} - \eta \frac{\partial e}{\partial w_{kh}} \tag{11}$$

$$\theta_k = \theta_k + \Delta \theta_k = \theta_k - \eta \frac{\partial e}{\partial \theta_k} \tag{12}$$

$\Delta\theta_k$ shows the variation of the connection weights between the $k$th neuron in the output layer and the $h$th neuron in the hidden layer.

Step 5: Similar to adjusting the connection weights and thresholds of the output layer, the error signal is back-propagated. The connection weights and thresholds of the hidden layer are adjusted based on the output error signal $e$.

$$\frac{\partial e}{\partial v_{hi}} = \frac{\partial e}{\partial y_k} \frac{\partial y_k}{\partial \beta_k} \frac{\partial \beta_k}{\partial b_h} \frac{\partial b_h}{\partial a_h} \frac{\partial a_h}{\partial v_{hi}} = y_k(1 - y_k)(\hat{y}_k - y_k) b_h(1 - b_h) x_i \sum_{k=1}^{n} w_{kh} \tag{13}$$

$$\frac{\partial e}{\partial \gamma_h} = \frac{\partial e}{\partial y_k} \frac{\partial y_k}{\partial \beta_k} \frac{\partial \beta_k}{\partial b_h} \frac{\partial b_h}{\partial \gamma_h} = -y_k(1 - y_k)(\hat{y}_k - y_k) b_h(1 - b_h) \sum_{k=1}^{n} w_{kh} \tag{14}$$

$$v_{hi} = v_{hi} - \eta \frac{\partial e}{\partial v_{hi}} \tag{15}$$

$$\gamma_h = \gamma_h - \eta \frac{\partial e}{\partial \gamma_h} \tag{16}$$

Step 6: Finally, update the connection weights and thresholds of the neural network and repeat steps 2 to 5 until the accuracy requirement is satisfied.

#### 2.2.2. PSO Optimization Algorithm

The PSO algorithm was first introduced by Eberhart and Kennedy and used for the optimization of continuous nonlinear functions [36]. The PSO algorithm is a population-based random optimization technique that simulates the process of bird and fish feeding in nature and searches for the global optimal solution to the problem through the collaboration of the population. The particles in the PSO algorithm have only two attributes, including velocity and position. Each particle searches for the optimal solution independently in the search space, which is recorded as the current individual optimal position $p_{\text{pbest}}$. The value of the optimization objective function is set to $f_{\text{p}}$. The particle shares its individual extreme value with the other particles in the whole particle swarm. The optimal individual extreme value is taken as the current global optimal position of the whole particle swarm $p_{\text{gbest}}$. The value of the optimization objective function is denoted as $f_{\text{g}}$. All particles in the particle swarm dynamically adjust their velocities and positions according to the current individual extreme values and the current global optimal solution shared by the whole swarm [37]. The particles update their positions and velocities according to the following equation:

$$v_{id}(k+1) = w v_{id}(k) + c_1 r_1 \left( p_{\text{pbest},id}(k) - x_{id}(k) \right) + c_2 r_2 \left( p_{\text{gbest},d}(k) - x_{id}(k) \right) \text{ and} \tag{17}$$

$$x_{id}(k+1) = x_{id}(k) + v_{id}(k+1), \tag{18}$$

where $i$ means the particle serial number; $d$ is the particle dimension number; $k$ is the number of iterations; $w$ is the inertia weight; $c_1$ is the individual learning factor, and $c_2$ is the population learning factor; and $r_1$ and $r_2$ are the random numbers in the range (0, 1), which are used to increase the randomness of the search. $v_{id}(k)$ denotes the velocity vector of the $d$th dimension for the particle $i$ during the $k$th iteration process. $x_{id}(k)$ presents the position vector of the $d$th dimension for the particle $i$ during the $k$th iteration process. Moreover, $p_{\text{pbest},id}$ is the individual optimal solution of the $d$th dimension for the particle $i$ during the $k$th iteration process, and $p_{\text{gbest},d}$ is the population optimal solution of the $d$th dimension for the population during the $k$th iteration process.

#### 2.2.3. PSO-BP Neural Network Construction

The biggest challenges for designing and training neural networks are the selection and determination of various hyperparameters, including the number of hidden layers, the number of neurons in each layer, the activation function, the training algorithm, the number of iterations, and the methods to prevent overfitting. In order to obtain the optimal hyperparameters of the PSO-BP neural network model conveniently and realize the adaptive adjustment and optimization of the network structure, the neuron number in the hidden layer, the iterations, the dropout regularization rate, and the training batch size of the BP neural network are optimized with the PSO algorithm in this paper. The construction process of the PSO-BP neural network is shown in Figure 2. The PSO-BP neural network is constructed based on the Google artificial intelligence system TensorFlow (version 2.10.0) in Python (version 3.9.16).

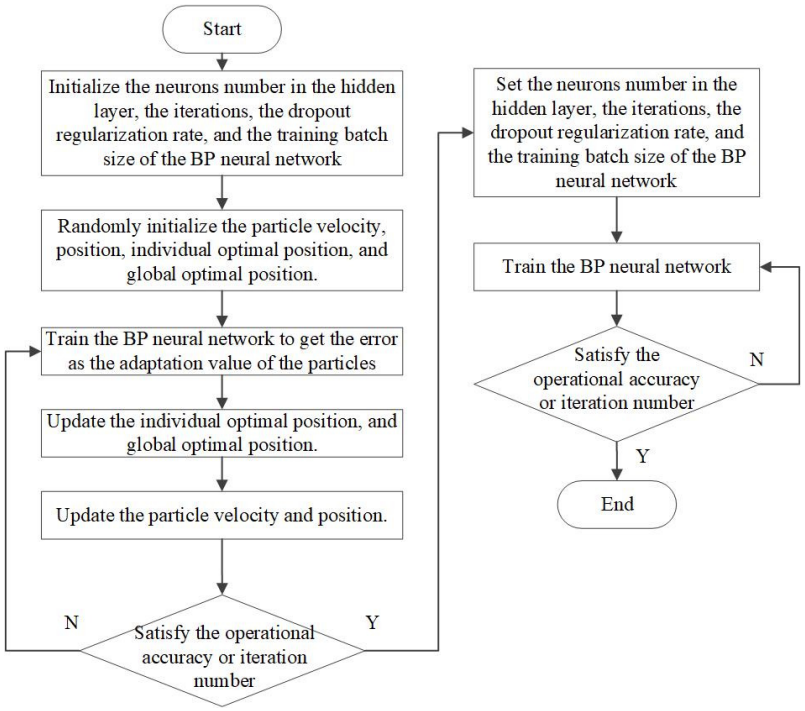


**Figure 2.** The construction process of the PSO-BP neural network.

## 3. Prediction of Anti-Icing Performance with the PSO-BP Neural Network

### *3.1. Dataset Preparation*

#### 3.1.1. Model and Cases for Anti-Icing Simulation

The parameters affecting the simulation results of the hot air anti-icing system can be categorized into external icing conditions and internal hot air anti-icing parameters. Flight tests have shown that aircraft icing conditions depend on several factors, including meteorological parameters like atmospheric temperature, cloud extent, MVD, and LWC; the flight status of the aircraft, such as flight height, flight speed, angle of attack, etc.; and the factors that determine the heat transfer characteristics of the flow in the hot air anti-icing cavity are mainly the flow, pressure, temperature of the bleed air jetted from the piccolo tube, and so on. The flight condition parameters of flight height, atmospheric temperature, and flight speed, represented by the Mach number later, MVD, and LWC, are taken as the input parameters of the fast prediction model, as shown in Figure 3. The angle of attack and the flow, pressure, and temperature of the bleed air jetted from the piccolo tube are the parameters directly related to flight speed and flight height according to the actual situation, which can be determined by interpolation calculation. The output parameters of the PSO-BP neural network include skin temperature and runback water distribution.

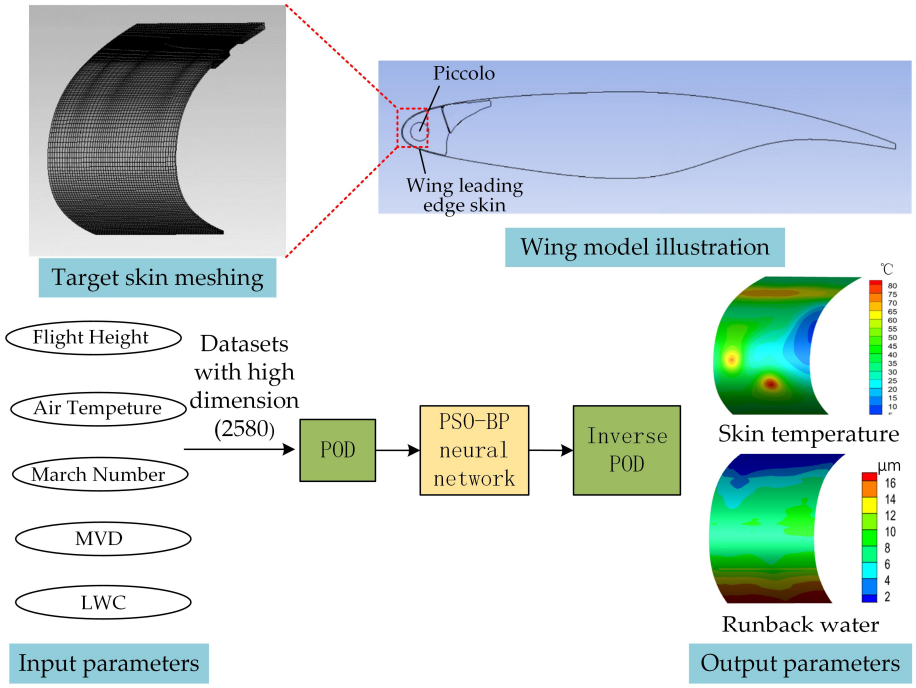


**Figure 3.** The model of the fast prediction for a wing's hot air anti-icing performance.

In the study, a part of the wing skin for a hot air anti-icing system is selected as the target research object, which is shown in Figure 3. The length of the wing chord and spanwise are 1.08 m and 0.08 m, and the thickness of the wing skin is 1.8 mm. The meshing result of the target wing skin (solid domain) turns out to be 82,831 grid nodes. The reliability of the meshing result for CFD simulation has been verified by previous engineering projects. The target skin surface has 2580 grid nodes, i.e., the dimension $p$ of a single simulation sample is 2580. The model of the hot air anti-icing system for CFD simulation is calibrated with the test data. Some of the test cases are displayed in Table 1. The numerical simulation is conducted under the same conditions as the test cases with FENSAP-ICE (version 19.2). FENSAP-ICE is used to simulate the anti-icing performance of a hot air anti-icing system, which is a commercial CFD software for icing and anti-icing calculation [38]. The difference between the simulation results and test data for surface temperature along the wing chordwise direction is illustrated in Figure 4. The values along the $x$-axis direction in Figure 4 indicate the distance between the target point and the stationary point, and the point where $x = 0$ means the stationary point position. The position where $x > 0$ is located on the upper surface of the airfoil, and the points with $x < 0$ lie on the lower surface. The results show that the difference between the CFD simulation data and the test data for the upper surface temperature is within 10 K, and the comparison results for the lower surface temperature are within 15 K. The maximum of the average temperature for all four cases in the direction of wing span is counted to be 9.98 K, which meets the CFD calculation accuracy requirements for engineering applications.

**Table 1.** Cases for anti-icing simulation model calibration.

| Case | Flight Height (ft) | T (°C) | March Number | MVD (μm) | LWC (g/m$^3$) |
|---|---|---|---|---|---|
| 1 | 10,473 | −6.9 | 0.44 | 13.9 | 0.288 |
| 2 | 10,773 | −7.5 | 0.42 | 15.6 | 0.375 |
| 3 | 11,000 | −8.1 | 0.41 | 16.8 | 0.400 |
| 4 | 13,115 | −10.8 | 0.45 | 15.0 | 0.298 |

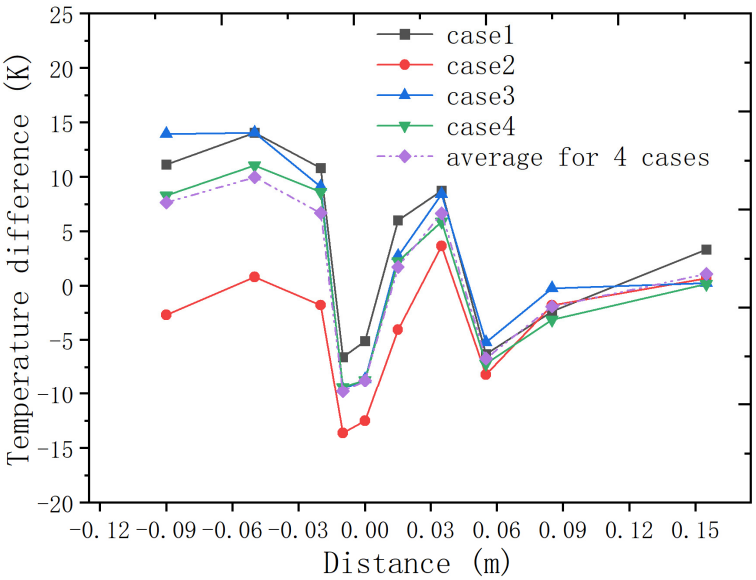


**Figure 4.** Temperature difference between the numerical simulations and experiments.

Homogeneous sampling is conducted within the parameter space of flight conditions, which is determined by the intersection of the limiting icing envelope, the relationship between icing meteorological conditions, and the flight envelope. To obtain a more representative dataset, appropriate encryption is applied when sampling the limiting icing envelope and the flight envelope. Then, 1434 uniformly distributed samples are obtained for model training and testing, and details of some cases are shown in Table 2.

**Table 2.** Flight icing conditions for some cases.

| Case | Flight Height (ft) | T (°C) | March Number | MVD (μm) | LWC (g/m$^3$) |
|---|---|---|---|---|---|
| 1 | 0 | 0 | 0.18 | 15 | 0.80 |
| ⋮ | ⋮ | ⋮ | ⋮ | ⋮ | ⋮ |
| 100 | 0 | −15 | 0.25 | 30 | 0.17 |
| ⋮ | ⋮ | ⋮ | ⋮ | ⋮ | ⋮ |
| 500 | 15,000 | −30 | 0.60 | 20 | 0.14 |
| ⋮ | ⋮ | ⋮ | ⋮ | ⋮ | ⋮ |
| 1434 | 31,000 | −40 | 0.82 | 50 | 0.05 |

The case sequence number increases from 1 to 1434 in increments of 1. The symbol of "⋮" means the conditions for some cases are omitted and not shown here.

### 3.1.2. Dataset Preparation with FENSAP-ICE

FENSAP-ICE is the second generation of icing and anti-icing analysis software, which applies modular thinking to separate and combine various steps of icing and anti-icing simulation to obtain different target results. Firstly, the external air flow field and internal flow field in the anti-icing cavity can be computed with the FENSAP-ICE module named FENSAP. The classical compressible Navier–Stokes equations are employed as the governing equation, which can be written in the following integral and conservative forms:

$$\frac{\partial}{\partial t}\int_{\Omega}\vec{W}_a d\Omega + \int_{\partial\Omega}(\vec{F}_{a,c} - \vec{F}_{a,v})dS = 0. \tag{19}$$

Then the droplet impingement properties are analyzed by the FENSAP-ICE module named DROP3D. The governing equations of the droplet impingement are based on the Eulerian model proposed by Bourgault [39]. This is essentially a two-fluid model

consisting of a set of Navier–Stokes equations augmented by droplet-related continuity and momentum equations. The local collection efficiency $\beta$ and the mass flow rate of impact water $\dot{m}_w$ can then be calculated as follows:

$$\beta = -\alpha \vec{u}_d \cdot \vec{n} \text{ and} \tag{20}$$

$$\dot{m}_w = LWC \cdot U_\infty \beta, \tag{21}$$

where $\vec{u}_d$ stands for the droplet velocity vector; $\alpha$ denotes the volume fraction, i.e., the proportion of volume occupied by water droplets in the control volume; and $U_\infty$ means the velocity of air flow in the far field. The shallow-water model is used in the FENSAP-ICE module named ICE3D to simulate surface water flow and heat transfer.

For the simulation calculation of a hot air anti-icing system, the FENSAP-ICE module named CHT3D is applied and adopts a loosely coupled method to exchange the data of the external flow field, the water film motion, the solid heat conduction, and the internal flow field. Then, the distribution of the skin temperature and runback water thickness after convergence can be obtained. The CHT3D module takes into account the energy balance relationship in the simulation process of anti-icing, as shown in Equation (22).

$$\dot{Q}_\mathrm{V} + \dot{Q}_\mathrm{F} = \dot{Q}_\mathrm{imp} + \dot{Q}_\mathrm{rad} + \dot{Q}_\mathrm{evap} + \dot{Q}_\mathrm{ice} + \dot{Q}_\mathrm{conv} + \dot{Q}_\mathrm{cond} \tag{22}$$

This indicates that energy change in the control body is caused by the heat flow of the impinging water $\dot{Q}_\mathrm{imp}$ the radiation heat flow $\dot{Q}_\mathrm{rad}$, the water evaporative heat flow $\dot{Q}_\mathrm{evap}$, the heat flow of the frozen water $\dot{Q}_\mathrm{ice}$, the heat flow of runback water $\dot{Q}_\mathrm{conv}$, and the heat flow of solid wall thermal conductivity $\dot{Q}_\mathrm{cond}$. Equation (22) is expressed in local differential form as follows:

$$\begin{aligned} \rho_w \left[ \tfrac{\partial h_f c_{p,w} \widetilde{T}}{\partial t} + div\left( \overline{u}_f h_f c_{p,w} \widetilde{T} \right) \right] \quad &= \left[ c_{p,w} \widetilde{T}_{d,\infty} + \tfrac{\overline{u}_d^{\,2}}{2} \right] \times U_\infty LWC\beta + \\ &\sigma\varepsilon\left( T_\infty^4 - T^4 \right) - \left[ \ldots \left( L_\mathrm{evap} + L_\mathrm{sub} \right) + c_{p,w} \widetilde{T} \right] \dot{m}_\mathrm{evap} + \\ &\left( L_\mathrm{fus} - c_{p,\mathrm{cee}} \widetilde{T} \right) \dot{m}_\mathrm{ice} + \dot{Q}_\mathrm{conv} + \dot{Q}_\mathrm{cond} \end{aligned} \tag{23}$$

where $\dot{Q}_\mathrm{cond}$ is obtained by thermal conductivity calculation; $\rho, c_f, c_s, \sigma, \varepsilon, L_\mathrm{evap}, L_\mathrm{fus}$ are the physical parameters of the fluid and solid wall; $T_\infty$ and $U_\infty$ are the temperature and velocity of the far-field air flow. $\dot{m}_\mathrm{evap}$ is the evaporated water mass flow rate, which is attained from $\dot{Q}_\mathrm{conv}$. $\dot{m}_\mathrm{ice}$ is the icing mass flow rate. $h_f$ is the water film thickness, and $T$ is the wall equilibrium temperature. The average time on CFD simulation for a case is about 3.5 h.

### *3.2. Fast Prediction Model of Hot Air Anti-Icing System Performance Based on POD and PSO-BP Neural Network*

In this paper, a fast prediction model for the performance of a hot air anti-icing system is established based on the abovementioned POD method and PSO-BP neural network. The whole process is as follows:

Step 1: Determine the input parameters with a number of $m$ and obtain $m$-dimensional vectors of flight condition parameters $\boldsymbol{V}^i = [x_{i1}, x_{i2}, \ldots, x_{im}],\ i = 1, 2, \ldots, n$ by data sampling homogeneously in the flight condition parameter space.

Step 2: Obtain the performance of the hot air anti-icing system by the simulation method in the target cases with the input parameters identified in the first step. If the grid number of the skin model is $p$, the skin temperature and runback water distribution samples of $p$ dimensions with a number of $n$ can be attained and recorded as $\boldsymbol{T}^i = [T_{i1}, T_{i2}, \ldots, T_{ip}]$ and $\boldsymbol{F}^i = [F_{i1}, F_{i2}, \ldots, F_{ip}]$, respectively.

Step 3: Reduce the dimensionality of the anti-icing performance parameter samples with the POD method. Then, we can get the first $q$-order basis modes $\boldsymbol{\psi}_T = \left\{\psi_T^1, \psi_T^2, \ldots, \psi_T^q\right\}$ and $\boldsymbol{\psi}_F = \left\{\boldsymbol{\psi}_F^1, \boldsymbol{\psi}_F^2, \ldots, \boldsymbol{\psi}_F^q\right\}$, which can reflect the characteristics of the skin temperature and runback water thickness distribution, and $q$-dimensional skin temperature samples $\boldsymbol{T}_{\mathrm{POD}}^i = [T_{\mathrm{POD},i1}, T_{\mathrm{POD},i2}, \ldots, T_{\mathrm{POD},iq}]$ and runback water thickness samples $\boldsymbol{F}_{\mathrm{POD}}^i = [F_{\mathrm{POD},i1}, F_{\mathrm{POD},i2}, \ldots, F_{\mathrm{POD},iq}]$ of characteristic coefficients with a number of $n$.

Step 4: The PSO-BP neural network is utilized to separately establish the mapping relationship for $\boldsymbol{V}^i$ and $\boldsymbol{T}_{\mathrm{POD}}^i$, as well as $\boldsymbol{V}^i$ and $\boldsymbol{F}_{\mathrm{POD}}^i$, respectively. The PSO-BP neural network models are established for each dimension of the characteristic coefficients. The skin temperature prediction models and runback water thickness prediction models can both be built with a number of $q$.

Step 5: After the training of the PSO-BP neural network models is completed, the flight condition parameters to be predicted $\boldsymbol{V}^{\mathrm{Predict}}$ can be fed into each PSO-BP neural network model. Then, we can achieve the characteristic coefficients of the skin temperature distribution $\boldsymbol{T}_{\mathrm{POD}}^{\mathrm{Predict}}$ and the runback water thickness $\boldsymbol{F}_{\mathrm{POD}}^{\mathrm{Predict}}$. Then, the inverse POD method can be used to obtain the skin temperature and runback water thickness, which allows for fast prediction of the anti-icing performance of the hot air anti-icing system.

In the study, the dimension of the skin temperature and runback water distribution samples $p$ is 2580, and the number of datasets $n$ is 1434. The number of input parameters $m$ is set to 5, which is the number of neurons in the input layer. The number of neurons in the output layer corresponds to the order of basis modes $q$ after the POD process, which turns out to be 10. The optimal values of hyperparameters in the multilayer neural network are shown in Table 3.

**Table 3.** The optimal values of hyperparameters for the PSO-BP neural network.

| Hyperparameter | Eigenvalues $\lambda_j$ |
|---|---|
| Number of the hidden layers | 4 |
| Number of neurons in the input layer | 5 |
| Number of neurons in the first hidden layer | 30 |
| Number of neurons in the second hidden layer | 64 |
| Number of neurons in the third hidden layer | 64 |
| Number of neurons in the fourth hidden layer | 30 |
| Number of neurons in the output layer | 10 |
| Activation function | ReLU |
| Loss function | MSE |
| Optimization algorithm | Adam Optimizer |
| Learning rate | 0.0001 |

### *3.3. Error Analysis*

In order to effectively evaluate the fitting effect of POD and the prediction effect of the PSO-BP neural network model, the mean absolute error (MAE) is used as the evaluation indices. The smaller the MAE is, the more accurate the model is. In this paper, the skin temperature and runback water thickness are the output values that we focus on. Therefore, the MAE of skin temperature and runback water thickness for a single sample are denoted as $\mathrm{MAE}_T$ and $\mathrm{MAE}_F$ as follows:

$$\begin{cases} \mathrm{MAE}_T = \dfrac{\sum_{i=1}^{p} \left| T_i - \hat{T}_l \right|}{p} \\ \mathrm{MAE}_F = \dfrac{\sum_{i=1}^{p} \left| f_i - \hat{f}_l \right|}{p} \end{cases} \tag{24}$$

where $T_i$ and $f_i$ are the skin temperature and runback water thickness obtained by numerical simulation at the $i$th grid point. $\hat{T}_l$ and $\hat{f}_l$ are the skin temperature and runback water

thickness attained from the POD fitting results or PSO-BP neural network prediction at the $i$th grid point, respectively. $p$ means the dimension of the single sample.

The error of the POD fitting model and the PSO-BP neural network prediction model is defined as the average error of all samples and calculated as follows:

$$\begin{cases} \text{Error}_T = \dfrac{\sum_{j=1}^{n} \text{MAE}_{T,j}}{n} \\ \text{Error}_F = \dfrac{\sum_{j=1}^{n} \text{MAE}_{F,j}}{n} \end{cases}, \tag{25}$$

where $\text{Error}_T$ and $\text{Error}_F$ are the fitting error or prediction error of the skin temperature and runback water thickness for all samples, respectively. $\text{MAE}_{T,j}$ and $\text{MAE}_{F,j}$ are the fitting error or prediction error of the skin temperature and runback water thickness for the $j$th sample. $n$ means the number of all samples.

## 4. Results and Discussion

### *4.1. POD Fitting Results*

The basis modes, eigenvalues, and occupied energy of the skin temperature distribution and the runback water thickness distribution are obtained by downscaling the sample data using the aforementioned POD method. The results are displayed in Tables 4 and 5. The variance contribution of a basis mode reflects the degree of the basis mode containing the sample characteristics. The cumulative variance contribution of the first 10 basis modes in the skin temperature datasets reaches 99.26%, while the cumulative variance contribution of the first 10 basis modes in the runback water thickness datasets is calculated to be 99.08%. The MAE of the skin temperature ($\text{MAE}_{T,\text{POD}}$) and runback water thickness $\text{MAE}_{F,\text{POD}}$ with the POD fitting method are illustrated in Figures 5 and 6. As the characteristics of the skin temperature distribution on the anti-icing surface are more easily captured, the average absolute error $\text{Error}_{T,\text{POD}}$ and average relative error between the simulation datasets and the skin temperature data after the POD and inverse POD processes are 1.65 K and 0.36% when selecting the first 10 basis modes, respectively. The distribution of runback water on the anti-icing surface is more complex than the temperature distribution. In the case of higher surface temperatures, the distribution area of runback water is very small or non-existent, making it more difficult to capture these characteristics. The average absolute error $\text{Error}_{F,POD}$ and the average relative error between the simulation datasets and the runback water thickness data after the POD and inverse POD processes are 0.42 μm and 6.28%, respectively, when selecting the first 10 basis modes.

**Table 4.** Eigenvalues and occupied energy for POD downscaling of skin temperature.

| Order | Eigenvalues $\lambda_j$ | Occupied Energy $E_j$ |
|---|---|---|
| 1 | 702,557.5495 | 0.7182 |
| 2 | 165,618.1213 | 0.1693 |
| 3 | 33,996.0586 | 0.0348 |
| 4 | 24,281.4796 | 0.0248 |
| 5 | 18,064.1157 | 0.0185 |
| 6 | 11,198.0621 | 0.0114 |
| 7 | 5171.1998 | 0.0053 |
| 8 | 4163.1418 | 0.0042 |
| 9 | 3474.4130 | 0.0036 |
| 10 | 2385.2014 | 0.0024 |

**Table 5.** Eigenvalues and occupied energy for POD downscaling of runback water thickness.

| Order | Eigenvalues $\lambda_j$ | Occupied Energy $E_j$ |
|---|---|---|
| 1 | 157,450.9476 | 0.8940 |
| 2 | 10,544.6952 | 0.0599 |
| 3 | 2160.2216 | 0.0123 |
| 4 | 1523.9089 | 0.0086 |
| 5 | 1054.4496 | 0.0060 |
| 6 | 492.1854 | 0.0028 |
| 7 | 437.2716 | 0.0025 |
| 8 | 347.1164 | 0.0020 |
| 9 | 251.6207 | 0.0014 |
| 10 | 216.2244 | 0.0012 |

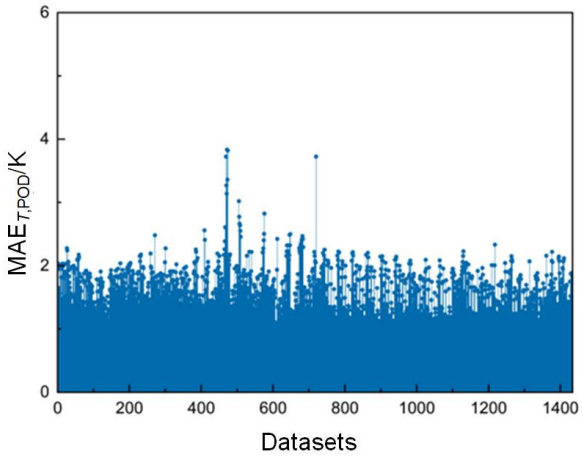


**Figure 5.** MAE of skin temperature with the POD fitting method.

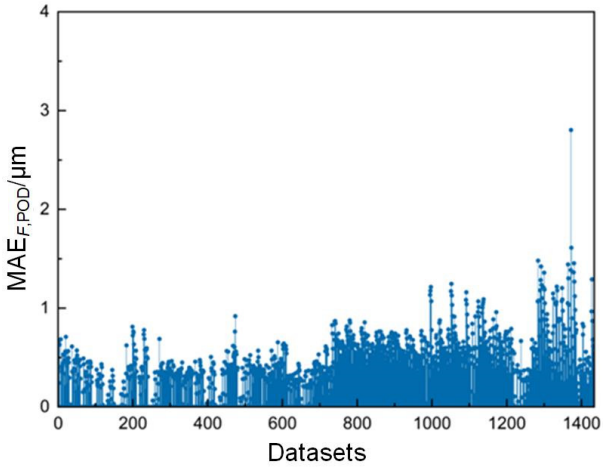


**Figure 6.** MAE of runback water thickness with the POD fitting method.

The first 10 orders of basis modes are used to fit the distribution of skin temperature and runback water thickness. The comparison of the POD fitting results with the CFD simulation results and the prediction errors for two of the training samples are shown in Figures 7 and 8. It can be seen that the POD fitting results and CFD simulation results are in good agreement, and the POD fitting results can accurately extract the characteristics of the skin temperature distribution and the thickness distribution of runback water. Figure 7b also demonstrates the power of the POD method to predict the runback water distribution when there is no water film on the skin surface.

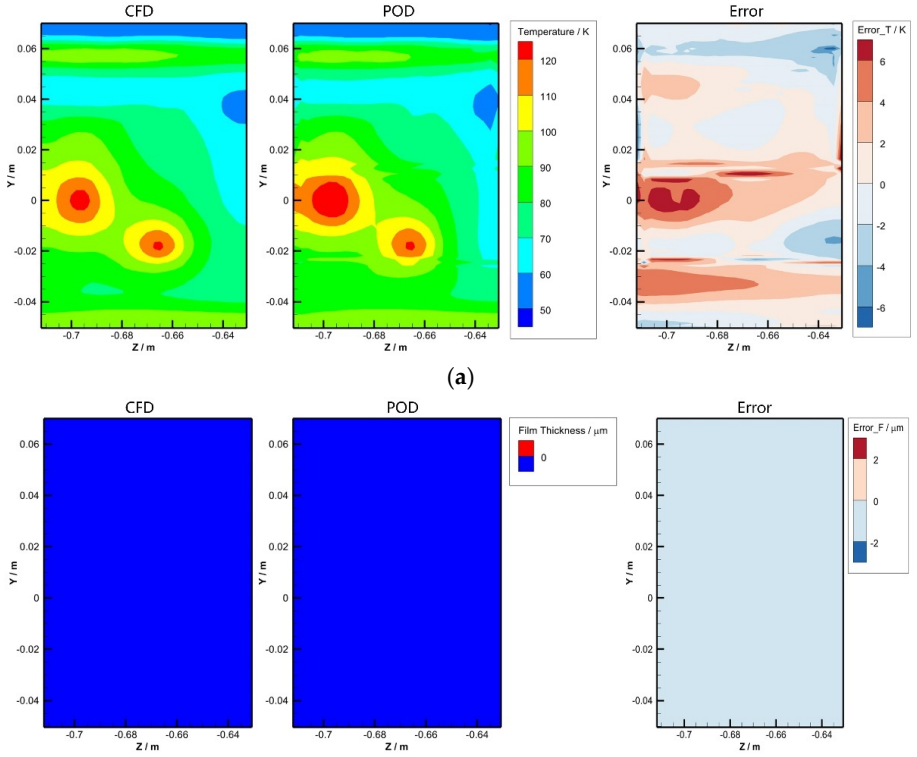


**Figure 7.** Comparison of the POD fitting results with the CFD simulation results (case 1): (**a**) skin temperature; (**b**) runback water thickness (no water film).

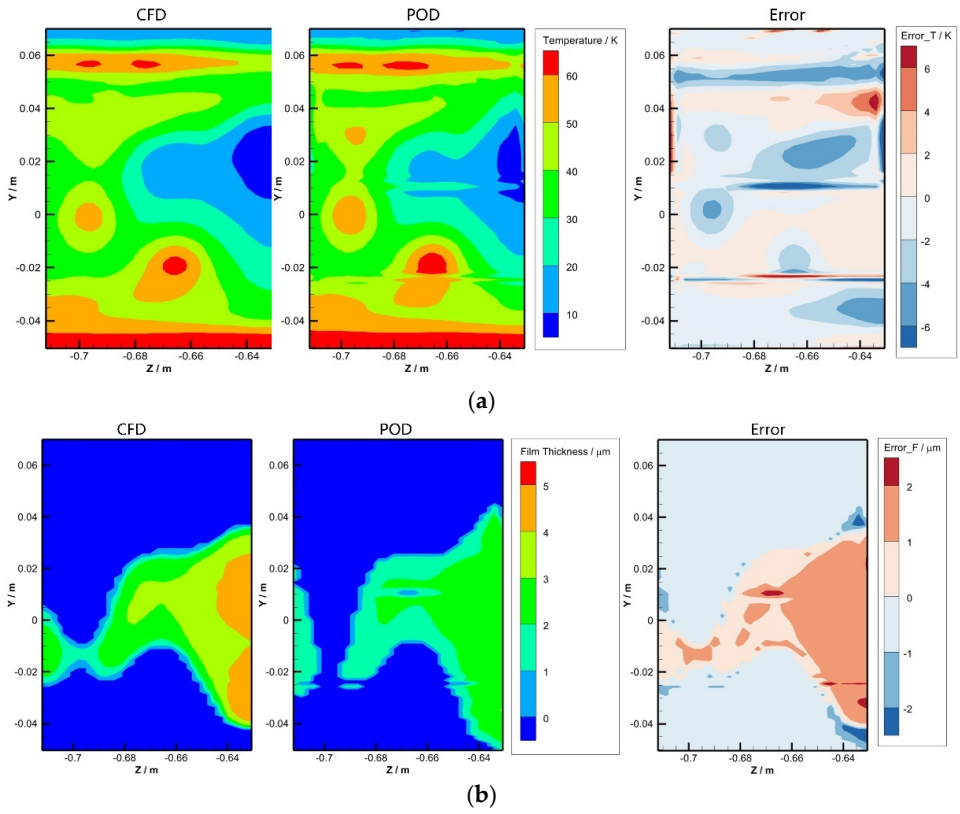


**Figure 8.** Comparison of the POD fitting results with the CFD simulation results (case 2): (**a**) skin temperature; (**b**) runback water thickness.

### *4.2. PSO-BP Neural Network Prediction Results*

According to the analysis in Section 4.1, the anti-icing performance of the hot air anti-icing system can be accurately predicted using the first 10 orders of POD basis modes. Therefore, PSO-BP neural network models with a number of 10 are established to rapidly predict the skin temperature and runback water thickness, i.e., setting up $\boldsymbol{V}^i$ and $\boldsymbol{X}_{\mathrm{POD},i1}$, $\boldsymbol{X}_{\mathrm{POD},i2}$,. . ., $\boldsymbol{X}_{\mathrm{POD},i1}$, respectively. After training the PSO-BP neural network models, the characteristic coefficients of the skin temperature distribution $\boldsymbol{T}_{\mathrm{POD}}^{\mathrm{Predict}}$ and the runback water thickness $\boldsymbol{F}_{\mathrm{POD}}^{\mathrm{Predict}}$ of 100 test samples can be predicted by the corresponding POS-BP models. The details of part of the 100 test samples for skin temperature prediction and runback water thickness prediction are displayed in Tables 6 and 7, respectively. The reverse Proper Orthogonal Decomposition (POD) method is used to predict the skin temperature and runback water thickness on 2580 grid nodes of the skin surface, enabling rapid prediction of wing anti-icing performance.

**Table 6.** Test samples of a fast prediction model for skin temperature distribution.

| Case | Flight Height (ft) | T (°C) | March Number | MVD (μm) | LWC (g/m$^3$) |
|---|---|---|---|---|---|
| 1 | 0 | −7.5 | 0.35 | 40 | 0.42 |
| ⋮ | ⋮ | ⋮ | ⋮ | ⋮ | ⋮ |
| 10 | 4000 | −5 | 0.35 | 25 | 1.55 |
| ⋮ | ⋮ | ⋮ | ⋮ | ⋮ | ⋮ |
| 40 | 19,000 | −30 | 0.50 | 45 | 0.16 |
| ⋮ | ⋮ | ⋮ | ⋮ | ⋮ | ⋮ |
| 100 | 32,000 | −30 | 0.60 | 35 | 0.05 |

The case sequence number increases from 1 to 100 in increments of 1. The symbol of "⋮" means the conditions for some cases are omitted and not shown here.

**Table 7.** Test samples of a fast prediction model for runback water thickness.

| Case | Flight Height (ft) | T (°C) | March Number | MVD (μm) | LWC (g/m$^3$) |
|---|---|---|---|---|---|
| 1 | 0 | 0 | 0.18 | 40 | 0.10 |
| ⋮ | ⋮ | ⋮ | ⋮ | ⋮ | ⋮ |
| 30 | 14,500 | −10 | 0.45 | 25 | 0.30 |
| ⋮ | ⋮ | ⋮ | ⋮ | ⋮ | ⋮ |
| 40 | 19,000 | −30 | 0.50 | 45 | 0.16 |
| ⋮ | ⋮ | ⋮ | ⋮ | ⋮ | ⋮ |
| 100 | 32,000 | -30 | 0.82 | 35 | 0.05 |

The case sequence number increases from 1 to 100 in increments of 1. The symbol of "⋮" means the conditions for some cases are omitted and not shown here.

Figures 9 and 10 demonstrate the mean absolute error MAE of skin temperature ($\mathrm{MAE}_{T,\mathrm{PSO\text{-}BP}}$) and runback water thickness ($\mathrm{MAE}_{F,\mathrm{PSO\text{-}BP}}$) obtained by comparing the PSO-BP neural network model and CFD simulation results for 100 test samples. The average absolute error $\mathrm{Error}_{T,\mathrm{PSO\text{-}BP}}$ of the PSO-BP neural network model in predicting skin temperature is 3.87 K for all test samples. The average absolute error $\mathrm{Error}_{F,\mathrm{PSO\text{-}BP}}$ of the PSO-BP neural network model to predict runback water thickness is 0.93 μm for all test samples. The prediction results for the anti-icing performance are of the same order of magnitude as those of the POD fitting results, indicating that the established fast prediction PSO-BP model is able to effectively predict the skin temperature and runback water thickness distribution characteristics on the skin surface of the hot air anti-icing system.

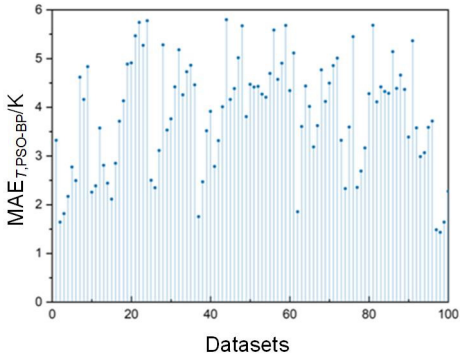


**Figure 9.** MAE of skin temperature with the PSO-BP neural network.

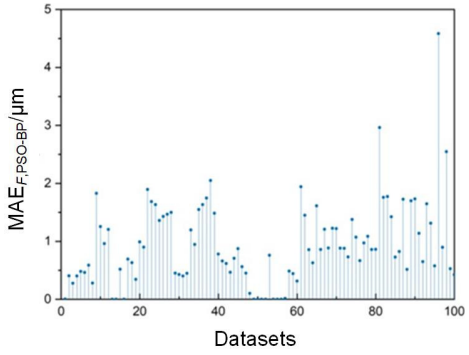


**Figure 10.** MAE of runback water thickness with the PSO-BP neural network.

Figures 11 and 12 display the prediction results of the PSO-BP neural network model and the CFD simulation results for two of the training samples, along with a comparison between these two sets of results. By synthetically analyzing the prediction effect of the fast prediction model, the established PSO-BP neural network can accurately predict the skin temperature and runback water thickness of the hot air anti-icing system. The PSO-BP neural network model can judge the distribution of runback water on the anti-icing surface. When the skin temperature is low and the thickness of the runback water is large, the model can accurately capture the distribution characteristics of the runback water. When there is only a small amount of runback water on the anti-icing surface or no runback water, the distribution characteristics are more difficult to capture. Furthermore, there is a possibility of a discrepancy in the prediction of the PSO-BP neural network model, which leads to a large prediction error.

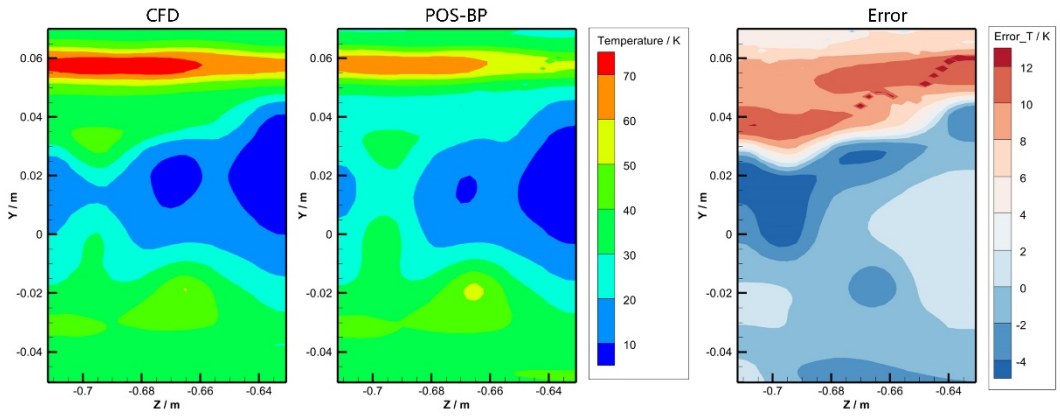


(**a**)

**Figure 10.** *Cont.*

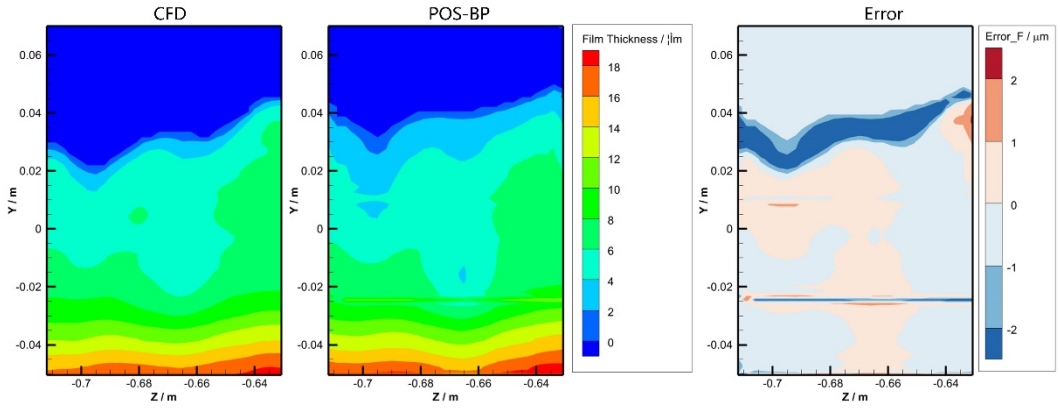


(**b**)

**Figure 11.** Comparison of the PSO-BP prediction results with the CFD simulation results (case 1): (**a**) skin temperature; (**b**) runback water thickness.

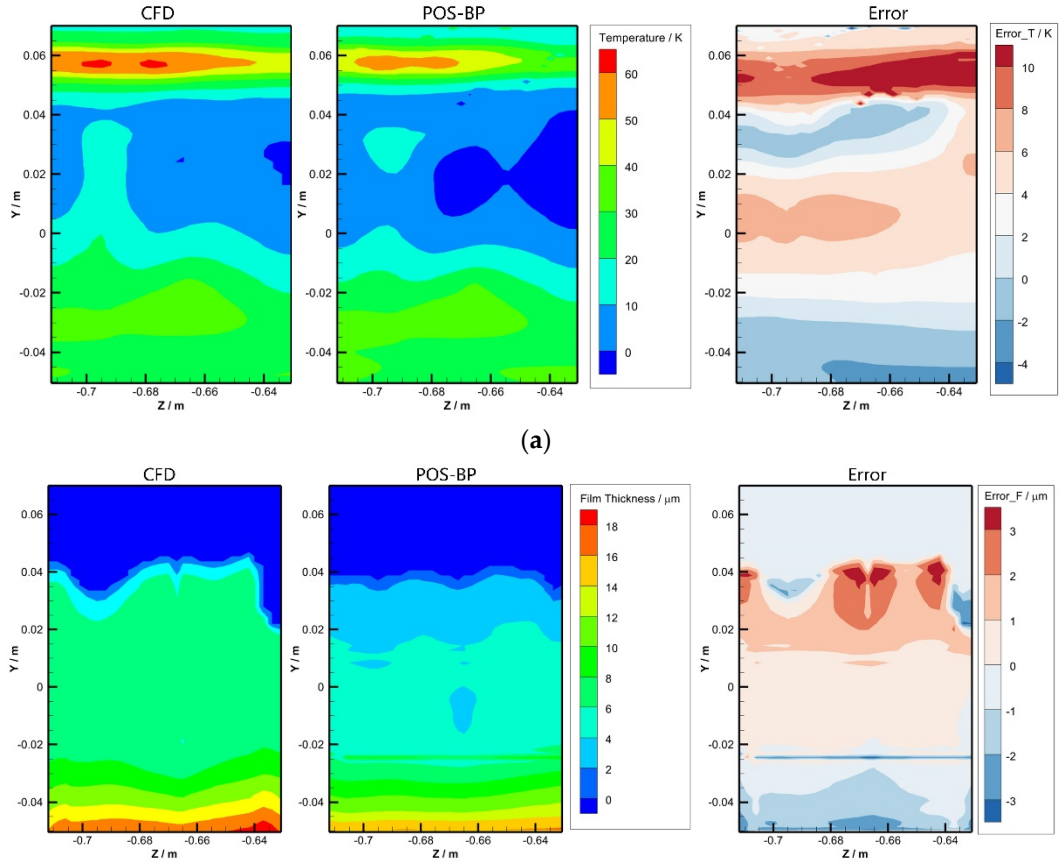


(**a**)

(**b**)

**Figure 12.** Comparison of the PSO-BP prediction results with the CFD simulation results (case 2): (**a**) skin temperature; (**b**) runback water thickness.

The model training and prediction process is conducted on a computer equipped with an Intel(R) Core (TM) i7-9700 3.00 GHz CPU (Intell®, Santa Clara, CA, USA). The results indicate that the time required for one model to train is around 10 min. The cost time of skin temperature prediction or runback water thickness prediction with the PSO-BP neural network and the process for output as a text file for a sample is 2.1255 s on average. Comparing with the average 3.5 h required for the CFD numerical simulation, the PSO-BP neural network significantly improves prediction efficiency and effectively resolves the

issues of high cost and long duration associated with the CFD numerical simulation of the hot air anti-icing system. This is achieved by reducing calculation complexity and the consumption of computing resources.

## 5. Conclusions

In this paper, a fast prediction method for the performance of a hot air anti-icing system based on the POD method and the PSO-BP neural network is established. The flight condition parameters, including flight height, atmospheric temperature, flight speed, MVD, and LWC, are used as input parameters for the fast prediction model. A dataset with a number of 1434 obtained by FENSP-ICE is applied to train and test the POS-BP neural network model. The prediction effect for rapidly predicting the skin temperature and runback water thickness distribution on the anti-icing surface is evaluated for a hot air anti-icing system. The conclusions are as follows:

- The POD method can accurately extract the skin temperature and runback water distribution characteristics of the anti-icing surface. The average absolute error $\text{Error}_{T,\text{POD}}$ and $\text{Error}_{F,\text{POD}}$ for the skin temperature and runback water thickness are 1.65 K and 0.42 μm when selecting the first 10 basis modes, respectively. It means that downscaling the sample data to obtain the basis modes, eigenvalues, and their occupied energies makes the fast prediction strategy feasible.
- The prediction results with the PSO-BP neural network show that the established model can more accurately predict the skin temperature and runback water thickness distribution characteristics of the hot air anti-icing system. The average absolute error $\text{Error}_{T,\text{PSO-BP}}$ and $\text{Error}_{F,\text{PSO-BP}}$ of the PSO-BP neural network model to predict skin temperature and runback water thickness are 3.87 K and 0.93 μm for all 100 test samples. The distribution of runback water thickness becomes more challenging to capture when there is only a small amount of runback water or none at all on the anti-icing surface. This leads to a more difficult prediction of the runback water thickness distribution.
- For cases requiring extensive performance analysis of a hot air anti-icing system, the model based on the POD method and the PSO-BP neural network can realize fast and accurate predictions of the performance of the hot air anti-icing system. This model holds high engineering application value and development potential due to its computational efficiency and accuracy.
- In the future, different neural networks, such as the convolutional neural network (CNN), will be implemented to construct the neural network framework for improved training results. Meanwhile, the wing anti-icing experiment data obtained from flight tests or wind tunnel tests will be fed into the training models as a more convincing training and testing dataset with high accuracy.

**Author Contributions:** Conceptualization, H.M., X.L. and X.S.; methodology, X.L. and W.Z.; software, H.M. and W.Z.; validation, Z.L.; formal analysis, X.L.; investigation, H.M.; resources, X.L. and H.M.; data curation, X.S. and Z.L.; writing—original draft preparation, X.L., H.M. and W.Z.; writing—review and editing, Z.L. and X.S.; visualization, H.M. and X.L.; supervision, Z.L.; project administration, Z.L. All authors have read and agreed to the published version of the manuscript.

**Funding:** This research received no external funding.

**Data Availability Statement:** The dataset is available upon request from the corresponding author. The data are not publicly available due to privacy.

**Conflicts of Interest:** The authors declare no conflicts of interest.

## Abbreviations

The following abbreviations are used in this manuscript:

| | |
|---|---|
| ANN | artificial neural network |
| BP | back propagation |
| CFD | Computational Fluid Dynamics |
| CNN | convolutional neural network |
| IoT | Internet of Things |
| LWC | liquid water content |
| MAE | mean absolute error |
| ML | machine learning |
| MVD | median volume diameter |
| POD | Proper Orthogonal Decomposition |
| PSO | Particle Swarm Optimization |
| WPT | wavelet packet transform |
| XGBoost | Extreme Gradient Boosting |

## References


1. Lynch, F.T.; Khodadoust, A. Effects of ice accretions on aircraft aerodynamics. *Prog. Aerosp. Sci.* **2001**, *37*, 669–767. [CrossRef]
2. Hamid, H.A.; Yong, W.K.; Yusoff, H.; Ismail, M. CFD Impingement Flow Study on Temperature Profile of Concave Plate. *Adv. Res. Fluid Mech. Therm. Sci.* **2022**, *95*, 1–16. [CrossRef]
3. Fukudome, K.; Tomita, Y.; Uranai, S.; Mamori, H.; Yamamoto, M. Evaluation of Anti-Icing Performance for an NACA0012 Airfoil with an Asymmetric Heating Surface. *Aerospace* **2021**, *8*, 294. [CrossRef]
4. Green, S. A study of US inflight icing accidents and incidents, 1978 to 2002. In Proceedings of the 44th AIAA Aerospace Sciences Meeting and Exhibit, Reno, NV, USA, 9 January 2006.
5. Papadakis, M.; Wong, S.H.; Yeong, H.W.; Wong, S.C.; Vu, G.T. Experimental investigation of a bleed air ice protection system. *SAE Trans.* **2007**, *116*, 643–663.
6. Brown, J.M.; Raghunathan, S.; Watterson, J.K.; Linton, A.J.; Riordon, D. Heat transfer correlation for anti-icing systems. *J. Aircr.* **2002**, *39*, 65–70. [CrossRef]
7. Myers, T.G. Extension to the Messinger model for aircraft icing. *AIAA J.* **2001**, *39*, 211–218. [CrossRef]
8. Lee, J.; Rigby, D.; Wright, W.; Choo, Y. Analysis of Thermal Ice Protection System (TIPS) with Piccolo Tube Using State-of-the-Art Software. In Proceedings of the 44th AIAA Aerospace Sciences Meeting and Exhibit, Reno, NV, USA, 9 January 2006.
9. Wang, H.; Tran, P.; Habashi, W.G.; Chen, Y.C.; Zhang, M.; Feng, L.J. Anti-icing simulation in wet air of a piccolo system using FENSAP-ICE. *SAE Trans.* **2007**, *116*, 715–723.
10. Thomas, S.K.; Cassoni, R.P.; MacArthur, C.D. Aircraft anti-icing and de-icing techniques and modeling. *J. Aircr.* **1996**, *33*, 841–854. [CrossRef]
11. Hinton, G.E.; Osindero, S.; Teh, Y.W. A fast learning algorithm for deep belief nets. *Neural Comput.* **2006**, *18*, 1527–1554. [CrossRef]
12. Johnstone, C.; Sulungu, E.D. Application of neural network in prediction of temperature: A review. *Neural Comput. Appl.* **2021**, *33*, 11487–11498. [CrossRef]
13. Smith, B.A.; McClendon, R.W.; Hoogenboom, G. An enhanced artificial neural network for air temperature prediction. *Int. J. Comput. Inf. Eng.* **2007**, *1*, 2166–2171.
14. Patil, K.; Deo, M.C. Prediction of daily sea surface temperature using efficient neural networks. *Ocean Dyn.* **2017**, *67*, 357–368. [CrossRef]
15. Sarkar, P.P.; Janardhan, P.; Roy, P. Prediction of sea surface temperatures using deep learning neural networks. *SN Appl. Sci.* **2020**, *2*, 1458. [CrossRef]
16. Wei, L.; Guan, L.; Qu, L.Q. Prediction of sea surface temperature in the South China Sea by artificial neural networks. *IEEE Geosci. Remote Sens. Lett.* **2019**, *17*, 558–562. [CrossRef]
17. Piotrowski, A.P.; Napiorkowski, M.J.; Napiorkowski, J.J.; Osuch, M. Comparing various artificial neural network types for water temperature prediction in rivers. *J. Hydrol.* **2015**, *529*, 302–315. [CrossRef]
18. Ma, Y.L.; Geng, Y.F.; Chen, X.H.; Lu, Y.X. Prediction for asphalt pavement water film thickness based on artificial neural network. *J. Southeast Univ. Engl. Ed* **2017**, *33*, 490–495.
19. Wang, B.; Chen, B.; Wang, G.; Li, R.; Wen, J.; Lu, C.; Tian, R.; Deng, J. Back propagation (BP) neural network prediction and chaotic characteristics analysis of free falling liquid film fluctuation on corrugated plate wall. *Ann. Nucl. Energy* **2020**, *148*, 107711. [CrossRef]
20. Ogretim, E.; Huebsch, W.; Shinn, A. Aircraft ice accretion prediction based on neural networks. *J. Aircr.* **2006**, *43*, 233–240. [CrossRef]
21. Chang, S.N.; Leng, M.Y.; Wu, H.W.; Thompson, J. Aircraft ice accretion prediction using neural network and wavelet packet transform. *Aircr. Eng. Aerosp. Technol. Int. J.* **2016**, *88*, 128–136. [CrossRef]

22. Yi, X.; Wang, Q.; Chai, C.C.; Guo, L. Prediction Model of Aircraft Icing Based on Deep Neural Network. *Trans. Nanjing Univ. Aeronaut. Astronaut.* **2021**, *38*, 535–544.
23. Strijhak, S.; Ryazanov, D.; Koshelev, K.; Ivanov, A. Neural network prediction for ice shapes on airfoils using icefoam simulations. *Aerospace* **2022**, *9*, 96. [CrossRef]
24. Dong, Y.Q. An application of deep neural networks to the in-flight parameter identification for detection and characterization of aircraft icing. *Aerosp. Sci. Technol.* **2018**, *77*, 34–49. [CrossRef]
25. Caliskan, F.; Aykan, R.; Hajiyev, C. Aircraft icing detection, identification, and reconfigurable control based on Kalman filtering and neural networks. *Aerosp. Eng.* **2008**, *21*, 51–60. [CrossRef]
26. Aykan, R.; Caliskan, F.; Hajiyev, C. F16 icing identification based on neural networks. *IFAC Proc. Vol.* **2004**, *37*, 201–206. [CrossRef]
27. Li, S.B.; Qin, J.K.; He, M.; Paoli, R. Fast evaluation of aircraft icing severity using machine learning based on XGBoost. *Aerospace* **2020**, *7*, 36. [CrossRef]
28. Cheng, X.; Shi, F.; Zhao, M.; Li, G.Y.; Zhang, H.X.; Chen, S.Y. Temporal attention convolutional neural network for estimation of icing probability on wind turbine blades. *IEEE Trans. Ind. Electron.* **2021**, *69*, 6371–6380. [CrossRef]
29. Abdelghany, E.S.; Farghaly, M.B.; Almalki, M.M.; Sarhan, H.H.; Essa, M.E.S.M. Machine learning and iot trends for intelligent prediction of aircraft wing anti-icing system temperature. *Aerospace* **2023**, *10*, 676. [CrossRef]
30. Yang, Q.; Guo, X.F.; Li, Q.; Dong, W. Hot air anti-icing performance estimation method based on POD and surrogate model. *Acta Aeronaut. Astronaut. Sin.* **2023**, *44*, 626992. (In Chinese)
31. Ostrowski, Z.; Białecki, R.A.; Kassab, A.J. Estimation of constant thermal conductivity by use of proper orthogonal decomposition. *Comput. Mech.* **2005**, *37*, 52–59. [CrossRef]
32. Cazemier, W.; Verstappen, R.; Veldman, A.E.P. Proper orthogonal decomposition and low-dimensional models for driven cavity flows. *Phys. Fluids* **1998**, *10*, 1685–1699. [CrossRef]
33. Lappo, V.; Habashi, W.G. POD-Kriging Approximations of Multi-Disciplinary CFD Simulation with Application to In-Flight Icing. In Proceedings of the 17th Annual Conference of the CFD Society of Canada, Ottawa, ON, Canada, 3–5 May 2009.
34. Jung, S.K.; Shin, S.; Myong, R.S.; Cho, T.H. An efficient CFD-based method for aircraft icing simulation using a reduced order model. *Mech. Sci. Technol.* **2011**, *25*, 703–711. [CrossRef]
35. Rumelhart, D.E.; Hinton, G.E.; Williams, R.J. Learning representations by back-propagating errors. *Nature* **1986**, *323*, 533–536. [CrossRef]
36. Kennedy, J.; Eberhart, R. Particle swarm optimization. In Proceedings of the ICNN'95-International Conference on Neural Networks, Perth, WA, Australia, 27 November–1 December 1995; IEEE: Piscataway, NJ, USA, 1995; Volume 4, pp. 1942–1948.
37. Xu, Y.S.; Zeng, B.; Yin, X.W. BP Neural Network and its applications based on improved PSO. *Comput. Eng. Appl.* **2009**, *45*, 233–235.
38. Beaugendre, H.; Morency, F.; Habashi, W.G. FENSAP-ICE's three-dimensional in-flight ice accretion module: ICE3D. *J. Aircr.* **2003**, *40*, 239–247. [CrossRef]
39. Bourgault, Y.; Habashi, W.G.; Dompierre, J.; Baruzzi, G.S. A finite element method study of Eulerian droplets Impingement models. *Int. J. Numer. Methods Fluids* **1999**, *29*, 429–449. [CrossRef]